Granular Matter (2023) 25:31
https://doi.org/10.1007/s10035-023-01314-1

ORIGINAL PAPER

Percolating contacts network and force chains during interface shear in granular media

Fernando Patino-Ramirez[1] · **Catherine O'Sullivan**[1] · **Daniele Dini**[2]

Received: 6 October 2022 / Accepted: 5 February 2023 / Published online: 23 March 2023

Abstract
The concept of force chains transmitting stress through granular materials is well established; however identification of individual force chains and the associated quantitative analysis is non-trivial. This paper proposes two algorithms to (1) find the network of percolating contacts that control the response of loaded granular media, and (2) decompose this network into the individual force chains that comprise it. The new framework is demonstrated considering data from discrete element method simulations of a ribbed interface moving against a granular sample. The subset of contacts in the material that transfers load across the sample, namely the percolating contact network (G_{perc}), is found using the maximum flow algorithm. The resulting network is fully-connected and its maximum flow value corresponds to the force percolating the system in the direction normal to the ribbed wall. G_{perc} re-orientates in response to the ribbed interface movement and transmits 85–95% of the stress, with only 40–65% of the contacts in the sample. Then, G_{perc} is split into individual force chains using a novel implementation of the widest path problem. Results show that denser materials with increased force-chain centrality promote a higher density of force chains, which results in a higher macro-scale strength during interface shearing. The contribution of force chains in the network is revealed to be highly centralized, composed by a small set of strong and long-lived force chains, plus a large set of weak and short-lived force chains.

Keywords Network analysis · Stress mobilisation · Fabric/structure of soils · Discrete element method

1 Introduction

The response of granular media to applied shear deformation or shear stress is controlled by a interconnected network of load-bearing contacts (usually referred as the strong contacts network) [1]. Based on this observation, [1, 2] proposed a partition of the contact network into strong/weak subnetworks, based on whether the magnitude of the contact force is above/below the mean force in the system. Developing upon this simple approach to partitioning authors have argued that the overall contact network is formed by 'primary' load-carrying contacts, and 'secondary' contacts that mostly provide lateral support [1, 3–7]. Various studies have found that the distribution of contact forces follows a power law with few contacts carrying high forces, and most contacts carrying relatively low forces [1, 6, 8–11], and this distribution is independent of pressure, sample size and particle size distribution [1, 12]. However, [13] found that this approach to partitioning is not mechanically robust, and using the mean force to differentiate strong and weak contacts is not always appropriate.

Recent studies have used graph theory, representing particles and contacts as nodes and edges [14], to propose partitioning methods based on the topology of the contacts. For instance, [15–17] used persistent homology to study tapped granular media, the compression of soft granular matter, and the stick–slip events in granular media (respectively). Community detection and clustering have been used to study granular materials in the context of sound transmission [18], deformation localisation [19, 20], kinematics [21] among many others.

✉ Fernando Patino-Ramirez
l.patino-ramirez@imperial.ac.uk

Catherine O'Sullivan
cath.osullivan@imperial.ac.uk

Daniele Dini
d.dini@imperial.ac.uk

[1] Department of Civil and Environmental Engineering, Imperial College London, London, UK

[2] Department of Mechanical Engineering, Imperial College London, London, UK

Flow networks (i.e. maximum flow and minimum-cut algorithms) have also been used to study the mechanical behaviour of granular media. [22, 23] applied the MFA to biaxially/triaxially loaded granular media, and found that the set of edges forming the bottleneck for force transmission in the system is located in the region of strain localisation (i.e., shear bands). Similarly, [24] developed a family of network flow models and used the MFA to find the percolating sub-network of contacts that transmits the highest units of force at least dissipated energy. These studies used expressions based on the local topology (3-cycle) and/or the magnitude of the relative displacement of the particles involved in the contact (edge) to set the capacity and/or cost of flow through each edge; effectively using the maximum flow as a relative measure of the force that could be transmitted through the contact network. Here we propose an algorithm that extends this capability, using the MFA on a directed network where the capacity of the edges is equal to the magnitude of the contact force in the direction of load transfer.

Other authors have found that the mechanical behavior of granular systems is controlled by the collective contribution of force chains, i.e. sets of particles that form 'column-like' structures that carry load [3, 5]. Methods used to identify force chains include 'geometric-mechanic' methods, which calculate the major principal stress orientation of the set of particles which is under above-average stress, and then defines force chains as the groups of particles which align with the principal stress orientation [25, 26]. Other 'similarity' methods use community detection, a clustering technique capable of finding chain-like structures in graphs [27]. Having identified individual force chains, prior researchers have studied force chain buckling [10], quantified their contribution to deviatoric stress [6], and tracked their temporal evolution [28–32].We propose an algorithm based on the widest-path problem to identify individual force chains from G_{perc} that collectively capture the force transmission across the granular media, and ultimately its mechanical response.

In this contribution we apply our developed algorithms to study the behaviour of granular media in contact with a rigid ribbed interface that applies a shear deformation in the direction of the initial major principal stress. This geometry and loading scenario has been used to measure soil properties in the laboratory [33] and for in-situ characterisation (using textured cone penetrometer sleeves) [34], and to study the seismic response of granular media inside gouges [35, 36]. These studies have found that the response of the interaction is controlled by the stress conditions, the density of the sample, and the relationship between particle size and the size of the ribs in the rigid body. Based on these observations, the dataset was developed using DEM to test the influence of different stress conditions and with different grain sizes.

2 DEM model

The dataset considered in this study was developed by simulating a ribbed interface moving against a granular material at a constant velocity. The texture morphology illustrated in Fig. 1d was developed following work by [37–40], In the current context, the role of the data generated are to illustrate the new methods developed herein.

The DEM models were built using the molecular dynamics code LAMMPS [41]. The simplified Hertz-Mindlin contact model was used [42], the particle shear modulus $G = 29\,\text{GPa}$, the Poisson's ratio $\nu = 0.12$, and the particle density $\rho = 2600\,\text{kg}\,\text{m}^{-3}$, are consistent with the properties of quartz. The use of spherical particles enabled large systems to be studied and minimize boundary effects. We acknowledge that excessive rotation of spheres does lead to a lower shear strength in comparison with sands. However, simulations using spheres capture key aspects of soil behaviour, e.g. the state dependency of strength and dilation, phase transformation, etc., as discussed in [43, 44].

To showcase the developed algorithms a parametric study was designed to consider a wide range of stress conditions and particle sizes to assess their influence in the response of the system. A total of 27 (3^3) simulations were performed, combining three particle size distributions, three vertical stresses (σ'_v : 50, 100, 150 kPa), and three particle friction coefficients during preparation (μ_p : 0.01, 0.1, 0.25). The preparation particle friction coefficient (μ_p) determined the density and initial anisotropy of the samples. The particle size distributions (PSD) were scaled (scaling factor $k = 1, 2, 4$) from the PSD of Toyoura sand, a fine rounded sand with a mean particle size $d_{50} = 0.22\,\text{mm}$, coefficient of curvature $C_c = 0.96$ and coefficient of uniformity $C_u = 1.39$ [45]. The resulting PSD's, referred herein as PSD_{std}, PSD_{mid} and PSD_{lrg}, have median particle diameters (d_{50}) of 0.22, 0.44, and 0.88 mm respectively.

The sample creation process is illustrated in Fig. 1. The width of the model (W_m) was set to: $W_m = h_r + 50 \cdot d_{50}$, while the depth was set to $D_m = 15 \cdot d_{50}$, where d_{50} is the median particle diameter in the samples. The sample size ($H_m \times W_m \times D_m$) was achieved with copies of a random cubic sample of side $15 \times d_{50}$ (see Fig. 1c). Random sphere packings yield relatively loose samples, therefore, an extra densification step was included to reduce the void ratio of the initial cubic sample, and with it, reduce the computational cost required to reach the desired confinement stress. In the first step, the spherical particles were placed randomly to create a cubic sample with a void ratio $e = 1.0$ (see Fig. 1a). In this initial stage, the diameter of each particle was sampled from the target PSD, and reduced

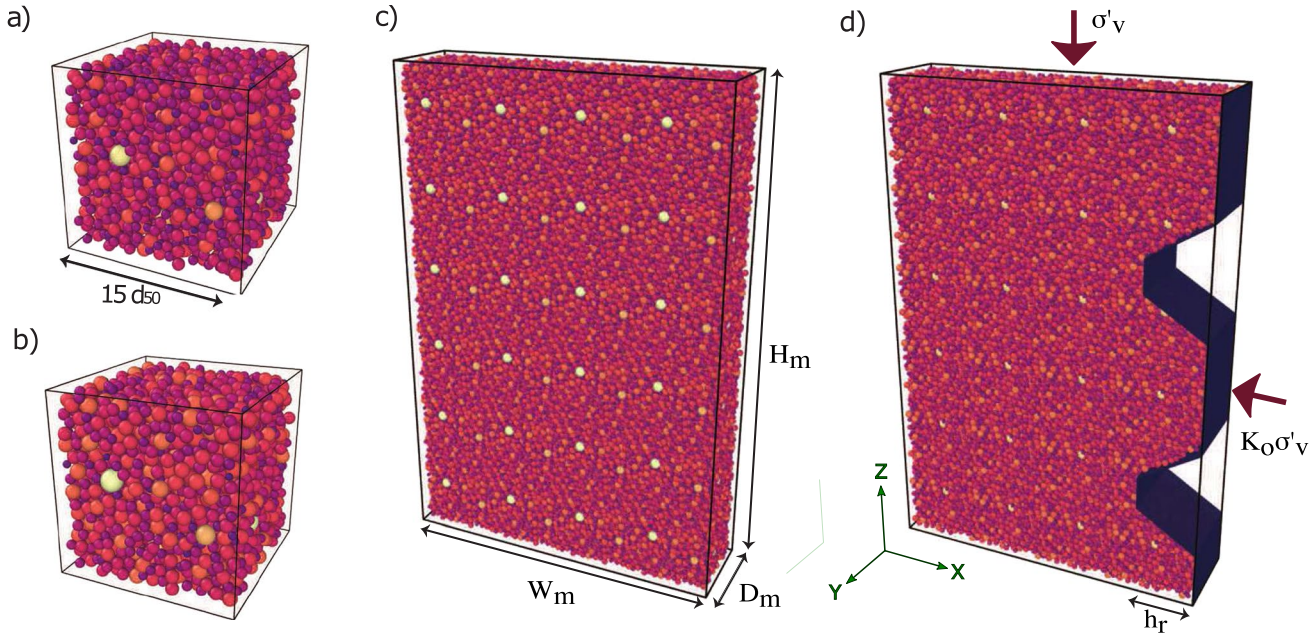

Fig. 1 Sample preparation. **a** Random cubic sample with reduced PSD. **b** Random cubic sample with target PSD. **c** Tiled sample. **d** Final sample with ribbed wall. Example shown for PSD_{mid} and $\mu_p = 0.25$

Table 1 Particle size, domain size, number of particles and inertial numbers of the simulations for the different PSD tested

	PSD_{std}	PSD_{mid}	PSD_{lrg}
d_{50} (mm)	0.22	0.44	0.88
W_m (mm)	16.7	26.9	54.1
H_m (mm)	33.4	31.1	32.6
D_m (mm)	3.6	7.3	14.7
Wall particles	51,840	25,680	13,298
Sample particles	190,809	73,934	40,818
Timestep (s)	3e−8	8e−8	1.5e−7
Inertial number (–)	$\leq 6.33 \times 10^{-4}$	$\leq 7.60 \times 10^{-4}$	$\leq 1.42 \times 10^{-3}$

by a factor of 1.2 prior to its placement. In the second step, a simulation was set up to incrementally increase the diameter of the particles in the cubic sample until they equalled the original diameters sampled from the PSD (see Fig. 1b). After this step, the cubic sample had a new void ratio $e = 0.67$. In the third step, copies of the cubic sample were tiled to reach the desired sample dimensions (see Fig. 1c). Lastly, the sample and the ribbed wall were merged, and any particles overlapping or penetrating the ribbed interface (described below) were removed (see Fig. 1d). A summary of the dimensions of the DEM models are shown in Table 1 where the values of H_m correspond to the densest scenarios ($\mu_p = 0.01$, $\sigma'_v = 150$ kPa).

Planar periodic boundaries were inserted at the top and bottom of the sample (i.e. at the minimum and maximum z values) and at the front and back of the sample (i.e. at the minimum and maximum y values). The left boundary wall (parallel to the yz plane at $x = 0$) was a planar rigid wall. A rigid, textured interface was inserted at the right hand side of the sample (i.e. the maximum values of x). The ribbed interface comprised wall particles with a diameter $d_w = d_{min}/2$, where d_{min} is the minimum particle diameter the simulated sample. These particles were placed on a square grid with a centre-to-centre spacing of d_w and there were no bonds or interactions between them. The heights of the trapezoidal ribs ($h_r = 5$ mm) correspond to about 23, 11 and 6 times d_{50} for each PSD tested; these values are sufficient to generate texture clogging and induce particle-to-particle shear response [46]. The ribbed geometry follows [34, 46], comprising alternating trapezoidal ribs with a height $h_r = 5$ mm and flat sections, with a length of 9 mm each. The wall includes two rib-flat sections, for a height of 36 mm, plus an additional flat region (added to account for sample compression during confinement) of 4 mm on top for a total sample height $H_m = 40$ mm. The number of wall and sample particles for the different PSDs tested are shown in Table 1.

After sample preparation, the models were allowed to reach equilibrium to remove any initial overlap between particles, after which residual stresses were negligible. Then, a servo-control mechanism was used to confine the sample particles by adjusting the position of the top periodic boundary (parallel to the z-direction) until the target vertical effective stress value (σ'_v) was reached. The dimensions of the samples along the

x- and y-directions remained unchanged during the simulation—therefore, the horizontal (x-axis) stress in the samples is consistent with K_0 stress conditions (see Fig. 1d). Gravity was not considered in the simulations. The displacement of the vertical boundary did not affect the wall particles that make up the textured rigid wall. The vertical strains induced during this stress-controlled confinement, ε_{zz}, ranged between 4.53% (for PSD_{std}, $\mu_p = 0.25, \sigma'_v = 50$ kPa), and 13.48% (for PSD_{mid}, $\mu_p = 0.01, \sigma'_v = 150$ kPa).

Once the target σ'_v was reached, the particle friction coefficient was changed to $\mu_s = 0.25$, and kept constant during wall movement. To simulate interface shear, the ribbed interface was displaced vertically (i.e. in the z-direction, see Fig. 3a) at a velocity $V_z = 25\,\text{mms}^{-1}$. During the interface shear the wall particles behaved as a rigid body moving at constant velocity. The chosen velocity is similar to the penetration speed of cone penetrometers [37]. Following [47], the inertial number (I) was calculated as shown in Eq. 1.

$$I = \dot{\gamma} d_{50} \sqrt{\frac{\rho}{P}} \tag{1}$$

where $\dot{\gamma}$ is the strain rate, d_{50} is the median particle diameter of the material, ρ is the particle density (2600 kg m^{-3}), and P is the stress level in the material, taken as σ'_v. The strain rate is calculated according to [48, 49] as: $\dot{\gamma} = V_z / L_p$; where L_p is the width of the shear zone developed adjacent to the textured wall. The shear zone thickness was calculated using the bi-linear relationship between L_p (normalized with by d_{50}) and the d_{50} defined by [50]. Following that relationship together with observations of the extent of the shear zone in the simulations, conservative values of $L_p = 9, 7.5, 4 \times d_{50}$ were used for PSD_{std}, PSD_{mid} and PSD_{lrg} respectively. Obtained values of I range between 3.7×10^{-4} (for PSD_{std} and $\sigma'_v = 150$ kPa) and 1.4×10^{-3} (for PSD_{lrg} and $\sigma'_v = 50$ kPa). The total displacement was 36 mm, equal to the total height of the ribbed wall.

3 Stress-deformation response

The average stress in the granular assembly during shear deformation is calculated from the contact forces and particle velocities according to [51] as:

$$\sigma'_{ij} = \frac{1}{V} \sum_{c=1}^{N_c} f_i l_j + \frac{1}{V} \sum_{p=1}^{N_p} m_p v_i v_j \tag{2}$$

where V is the sample volume (excluding the volume of the textured wall), N_c, N_p are the total number of contacts and particles (respectively), f_i is the ith component of the contact force vector, l_j is the jth component of the branch vector that joints the centers of the particles forming contact c, and v_i is the ith component of the particle velocity. According to CPT interface friction simulations from [49], quasi-static conditions are expected or $I < 1 \times 10^{-2}$, as was the case here, however the dynamic component of the stress tensor (Eq. 2) was included in the calculations as a conservative measure. The magnitude of the dynamic component of stress remained < 5% of the static component.

The stress anisotropy in the samples is quantified with the lateral earth pressure coefficient $K_0 = \sigma'_{xx} / \sigma'_{zz}$, where σ'_{kk} is the normal component of stress in the direction of the k axis, calculated from Eq. 2. The inter-particle friction coefficient during initial compression (μ_p) determined both the void ratio and initial stress anisotropy of the samples, with higher values of μ_p promoting higher void ratios (lower packing density)—ranging between 0.35 and 0.40, and increased stress anisotropy following the initial sample consolidation, with K_0 values between 0.65 and 0.91. The average values of e and K_0 for different values of μ_p are summarised in Table 2.

The overall stress response during shear deformation, shown in Fig. 2, is quantified in terms of the mobilised stress ratio q_{eq}/p', where the mean effective stress p' is calculated as $p' = \frac{1}{3} tr(\sigma') = \frac{1}{3} \sum \sigma'_{ii}$ and the equivalent deviatoric stress is calculated as $q_{eq} = \sqrt{3 J_2}$, where J_2 is the second invariant of the deviatoric stress tensor $\sigma'_{dev} = \sigma' - p' I$, calculated as $J_2 = \frac{1}{3} tr((\sigma'_{dev})^2)$.

The particle friction coefficient during preparation μ_p, is the variable with the biggest influence in the stress mobilisation in the system, as it controls the density of the material (in terms of e), and the stress in the x-direction σ'_{xx} (and hence K_0). Higher mobilised stress ratios (q_{eq}/p') were obtained for denser samples and higher values of K_0. Moreover, these dense, anisotropic samples reach a steady state at significantly larger wall displacements; arguably even longer than the 36 mm of displacement tested in the simulations. These results are in agreement with the sleeve friction during CPT testing [52–55], and with results from interface friction with ribbed walls of similar geometry to this study [38–40].

The small increase in q_{eq}/p' (and its fluctuations) with PSD, is a phenomenon that has been attributed to particle size effects, and to changes in the relative roughness ($R_r = h_r / d_{50}$) of the ribbed wall. Butlanska et al. [56] modeled CPT tests with scaled PSD and found that the increase in the magnitude of the fluctuations of the soil response is related to the decrease in the number of particles in contact with the rigid surface. While [38] studied ribbed walls with the same geometry, and suggested that for higher R_r values the relatively small particles clog and mobilise the particle-particle shearing resistance,

Table 2 Mean void ratio e and lateral earth pressure coefficient K_o for different values of μ_p

μ_p	0.25	0.10	0.01
e	0.395	0.379	0.357
K_o	0.675	0.732	0.898

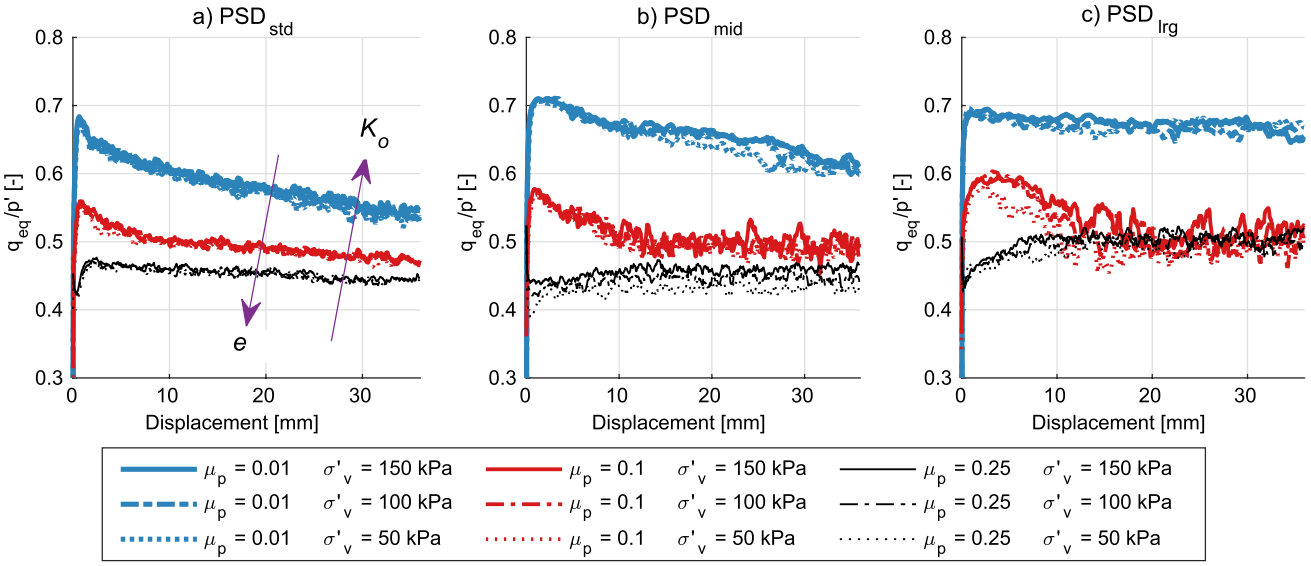

Fig. 2 Mobilised stress ratio q_{eq}/p' as a function of wall displacement for the three particle size distributions considered. The stress data were calculated considering the sample particles (i.e. excluding the wall particles)

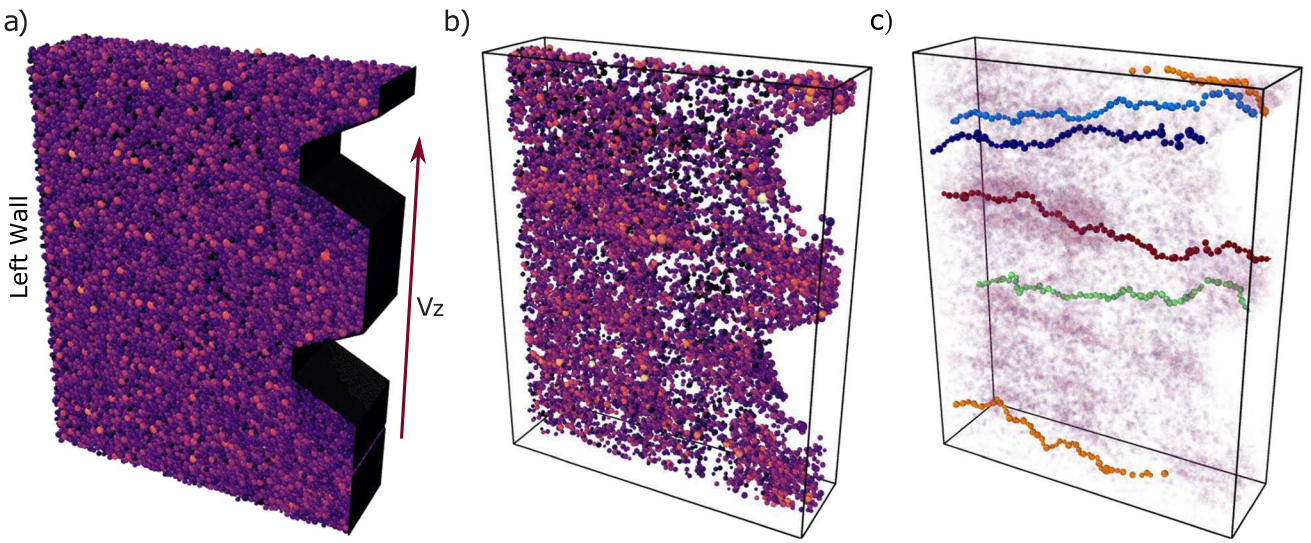

Fig. 3 Example model, percolating network and strongest force chains for a test with PSD_{mid}, $\mu_p = 0.25$ and $\sigma'_v = 50kPa$. **a** Complete sample, **b** particles that belong to the percolating network G_{perc}, and **c** five strongest force chains in G_{perc}

while in the case of lower R_r values, the larger particles are less prone to clogging and can therefore mobilise additional passive resistances during shear. σ'_v has little influence in q_{eq}/p', with tests on samples with a similar μ_p and PSD but different σ'_v showing a similar response.

4 Percolating contacts network

In contrast to direct shear laboratory tests where the major principal stress is normal to the shearing direction, for the dataset considered here the shearing direction (z-axis) is parallel to the major principal stress orientation. Previous studies considering similar loading conditions [34, 37, 46] have shown that the response of the system is controlled by the force chains normal to the shearing direction, i.e. the x-direction in the current study. In this section, we propose a new method to partition the contact network into two complimentary sub-networks: (1) a principal network that transmits the force percolating through the sample in the x-direction, namely the percolating network G_{perc}, and (2) a secondary contact network formed by the remaining particles and contacts that support the structure of the material

but do not contribute directly to the force transmission in the x-direction, namely the supporting network G_{supp}.

The partition of the contact network is achieved using network analysis. Particles and contacts in the samples are represented as nodes and edges (respectively) in a directed graph G, as described by [14]. The node (particle) information includes the particle diameter, position (x,y,z coordinates), coordination number (equivalent to the node degree in graph theory) and type (i.e wall or sample particle). The edge (contact) information includes the IDs of the particles forming the contact, and the force components (normal and tangential). The edge direction is set such that the contacts are oriented from the ribbed wall towards the planar rigid wall at $x = 0$ (i.e. the left wall see Fig. 3a which shows the complete sample) as:

$$c : \begin{cases} (j,i), \text{ if } \quad x_j > x_i. \\ (i,j), \text{ otherwise.} \end{cases} \tag{3}$$

where x_i is the x-coordinate of node i, and the contact $c(i,j)$ is oriented from node i to node j.

The percolating network G_{perc} is found using the maximum flow algorithm (MFA). Finding the maximum flow between a source s and a target t node in a graph with edges of finite capacity is a classical problem in optimisation theory [57]. The solution involves finding the set of paths connecting s, t which form the bottleneck of flow in the network. Adopting this approach ensures that: (1) the flow through each edge in the graph does not exceed its capacity, (2) at every node (other than s and t) the values of in-flow and out-flow are equal, i.e. mass balance is preserved, and (3) no extra paths or extra flow can be added to the solution without violating the previous conditions.

The response of the system is controlled by the force transmission in the x-direction, therefore, the capacity C_ϵ of edge ϵ in the algorithm was set to the x-component of its contact force, namely $C_\epsilon = |f_x^n + f_x^t|$, where f_x^n and f_x^n are the x- components of the normal and tangential forces. In this way, the flow through ϵ corresponds to the percolating force transmitted by that given contact, and is $\leq C_\epsilon$. Virtual nodes were added to represent the ribbed interface (source s) and the opposite left wall at $x = 0$ (target t). Next, artificial edges of infinite capacity were added from s, to every wall particle, and from t to every particle in contact with the left wall. In this way, the algorithm captures all the paths of force transition in the x-direction between the left wall and the ribbed interface. Then, MATLAB's [58] implementation of the Edmonds–Karp's maximum flow algorithm [57] was used to find the maximum flow network and its maximum flow value.

The maximum flow value corresponds to the total percolating force in the sample in the x-direction, while the subset of edges (contacts) with non-zero flow (i.e. contacts that contribute to the percolating force) form the percolating network G_{perc}. The resulting G_{perc} is fully connected, meaning that for every pair of nodes (particles) in G_{perc}, a continuous path with non-zero percolating force exists. The mass-conservation principle of the algorithm ensures that the sum of the in-coming and out-going percolating forces on each particle (node) in G_{perc} are equal.

4.1 Characteristics of particles and contacts in the sub-networks

The characteristics of the sub-networks (G_{perc} and G_{supp}) are analysed for the interval $X_p = [0, 36]$ mm of wall displacement, with only minor changes to the characteristics of the sub-networks during the interval. In the following, representative characteristics of the system are shown for $X_p = 36$ mm. Figure 3b shows the particles in the percolating network G_{perc} for a representative sample.

Figure 4 summarises the proportion of particles, N_p, and contacts, N_c, in G_{perc} as a function of PSD and μ_p. G_{perc} contains between 40 and 60% of the total number of contacts in the network, and involves between 60 and 85% of the particles in the samples. The proportion of particles and contacts in G_{perc} increases with sample density (i.e. decreasing μ_p), and with increasing particle size. This observation suggests that denser materials, with larger particles create more pathways to percolate force in the system, this observation is verified later in the study of the force chains in the system (see Fig. 11).

Figure 5 shows the cumulative distribution functions (CDF) of the particle sizes, the contact forces f_c, and β (the ratio between the tangential and normal contact force) in G_{perc} and G_{supp}. The particle sizes and contact forces are normalised as percentiles for easier comparison between simulations, while β is shown in the range $[0, \mu_s]$ (where $\mu_s = 0.25$ is the inter-particle friction coefficient during shearing, equal for all simulations). Lines in Fig. 5 correspond to the mean CDF for all the simulations, while the interquartile range—IQR (i.e. the range between the 25th and 75th percentiles of the data) is shown as shaded regions. Due to the small differences between the CDF's in Fig. 5, the region enclosed by IQR is virtually indistinguishable from the mean lines.

The results show that G_{perc} is formed by larger diameter particles and contact forces than G_{supp}. However, both sub-networks contain particles of every size and contacts forces of every strength, rather than exclusively small/big particles or weak/strong contact forces, as suggested by a-priori partition techniques based on contact force [9, 22, 59]. The distribution of β shows that, on average, contacts in G_{supp} are closer to sliding than those in G_{perc}, with 38% sliding contacts in G_{supp} and 26% sliding contacts in G_{perc}; similar results have been observed by [1, 59].

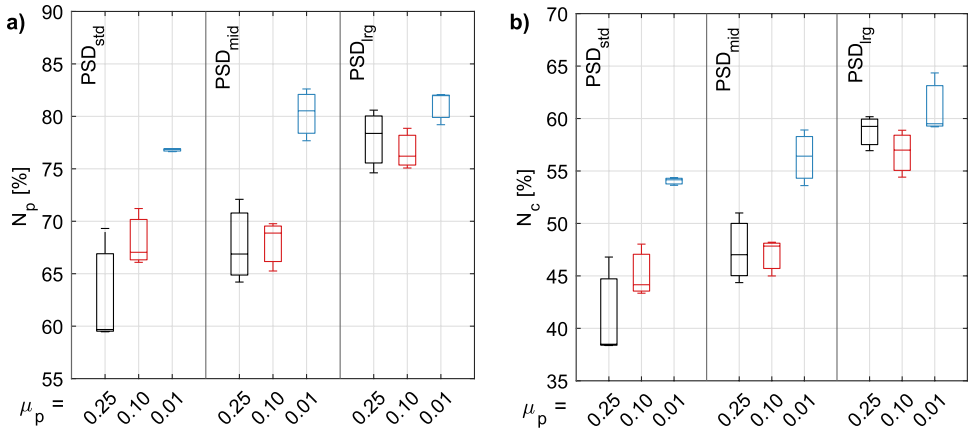

Fig. 4 Percentage of particles N_p, contacts N_c, in the percolating network G_{perc}. Each boxplot represents the distribution of the quantity over the simulations with the same μ_p, PSD

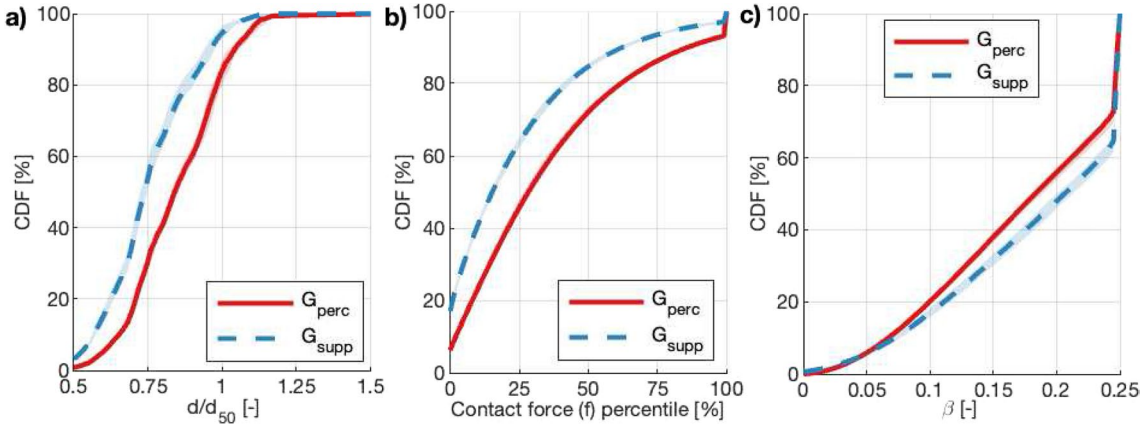

Fig. 5 Cumulative distributions of **a** (normalised) particle size *PSD*, **b** contact force f and **c** β (the ratio between the tangential and normal contact force). Lines show the mean value across simulations and shaded regions show the inter-quartile range (IQR), namely the range between the 25th and 75th percentiles of the data from the 27 simulations

4.2 Stress transmission in the sub-networks

The stress at steady state is measured from the stress tensor of the contact network at 36 mm of wall displacement, as before. The stress tensor of each sub-network, i.e. σ'_{perc} and σ'_{supp} is calculated according to Eq. 2, including only the particles and contacts in G_{perc} and G_{supp} respectively. For each tensor, three components of stress: the 2-norm of the stress tensor $\|\sigma'\|_2$ (equivalent to the major principal stress σ'_1), the isotropic stress (p'), and the deviatoric stress (q_{eq}) components are calculated. Figure 6 shows the distribution of each component of stress in G_{perc} relative to G. Results show that G_{perc} carries most (80–95%) of the stress in the material, while having only 40–60% of the contacts of the network. Moreover, the fraction of q_{eq} transmitted by G_{perc} appears to be slightly higher than the fraction of p' this partition transmits, although the difference is not significant. Previous studies on element tests based on strong and weak sub-networks [1, 5, 7], have also found (expectedly) that strong contacts (above the mean contact force in the system) carry most stress in the material.

Representative rose diagrams are presented on Fig. 7 for at simulation at 36 mm of wall displacement (similar rose diagrams were obtained for all simulations). The rose diagrams show significant differences in the preferential contact orientation amongst the sub-networks. G_{perc} has the strongest contacts in the network, and exhibits a preferred orientation between 35° and 55° (measured from the horizontal), which indicates a re-orientation of the contacts during wall movement. Conversely, contacts G_{supp} are weaker in comparison, and their preferred orientation is closer to 90°, i.e. close to the the vertical direction, consistent with the direction of the application of σ'_v.

The projection in the XZ-plane of the orientation of the major principal stress (α_1), is calculated as $\alpha_1 = \tan^{-1}(\eta_z/\eta_x)$, where η_x and η_z are the x and z components of η, the principal direction (eigenvector) associated with the major principal stress σ'_1. α_1 is calculated for G, G_{perc} and G_{supp}, and presented in Fig. 8, and as arrows in Fig. 7.

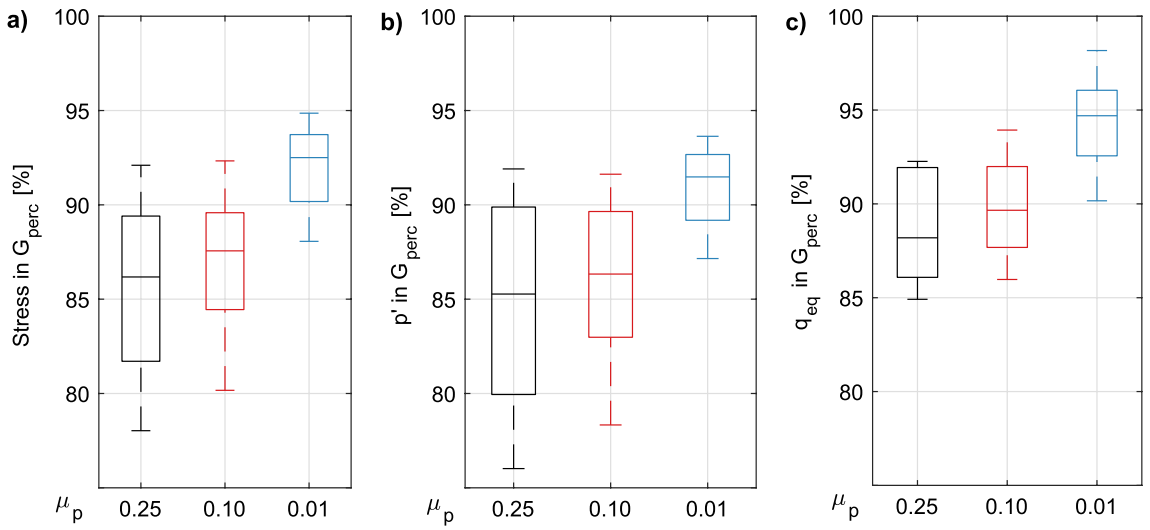

Fig. 6 Distributions of stress contributions of G_{perc}. **a** Fraction of stress magnitude (as 2-norm of stress tensor), **b** isotropic stress p', and **c** deviatoric stress q_{eq}, in G_{perc} relative to G. Each box-plot shows the distribution of the values for the 9 simulations with similar μ_p

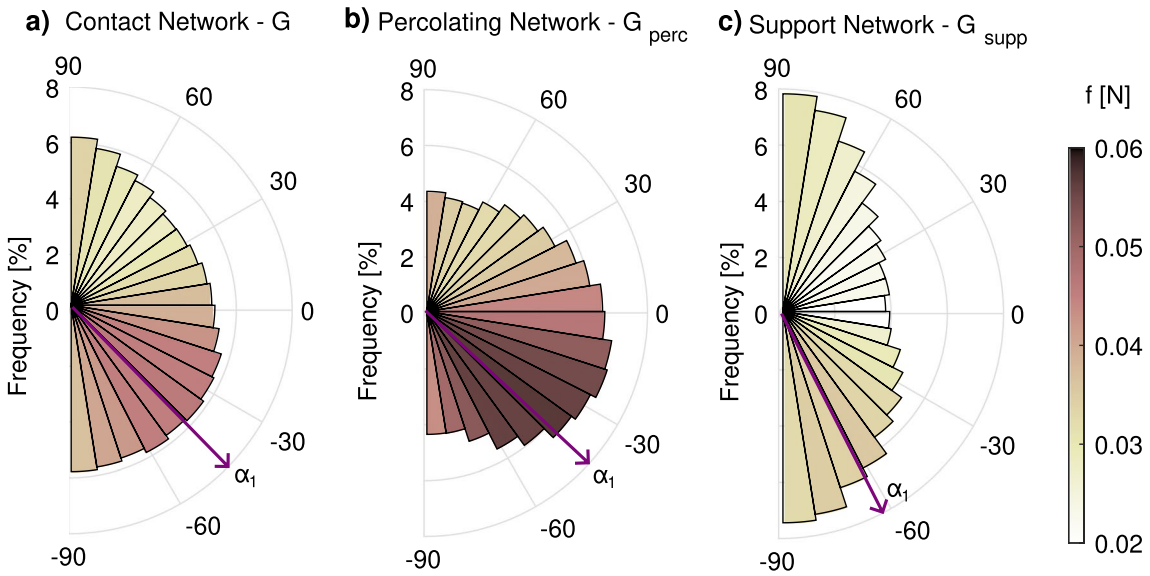

Fig. 7 Rose diagrams showing the frequency of the orientation of contacts (shown as percentage of the total amount of contacts in the network), shading of each bin is proportional to the average contact force magnitude among the contacts in the bin. Results shown for sample with PSD_{mid}, $\mu_p = 0.1$, and $\sigma'_v = 150\,\text{kPa}$, other simulations show comparable distributions

The results indicate that the displacement of the ribbed wall induces a rotation of the principal stresses in the material from its initial K_o state. This reorientation is reflected in the major principal stress orientation in G_{perc}, while G_{supp} remains oriented closer to the vertical direction, consistent with the rose diagrams shown on Fig. 7. Comparable results were encountered by [24, 59] during uniaxial loading, where the strong network re orientates in the direction of loading, while the weak network remains mostly unchanged.

4.3 Contact and particle importance

The relative importance of the particles and contacts in G_{perc} is measured in terms of node/edge centrality. The contact/edge centrality (C_{cen}) is the percentage of the total percolating force transmitted by each contact in G_{perc},

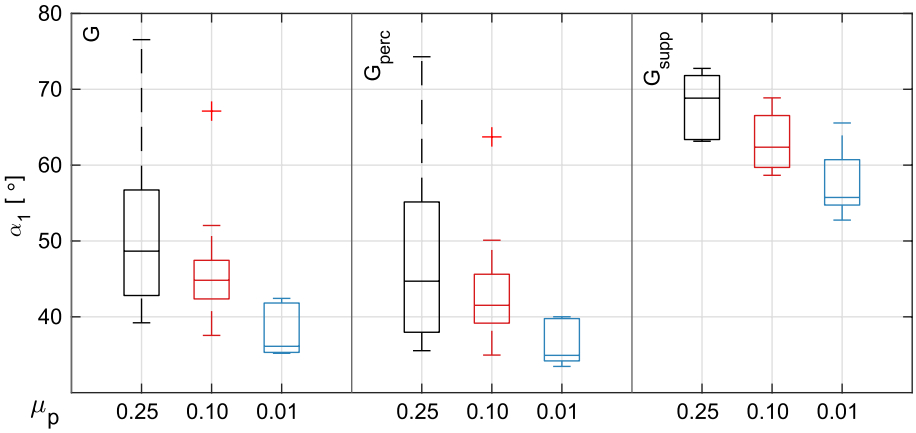

Fig. 8 Major principal stress orientation (α_1) in G, G_{perc} and G_{perc}. Orientation measured as the projection of the major principal direction of the stress tensor on the XZ plane. Values measured from the horizontal and positive in the clock-wise direction. Each box-plot shows the distribution of the values for the 9 simulations with similar μ_p

while the particle/node centrality (P_{cen}) is the percentage of the total percolating force transmitted through each particle. Centrality is grouped by percentiles, from the most (1st percentile) to the least (100th percentile) important groups of particles/contacts.

Figure 9 shows the distributions of $\overline{C_{cen}}$ (the mean contact C_{cen}), and $\overline{\beta}$ (the mean β at the contacts). The C_{cen} follows a exponential distribution, with few 'highly important' contacts. The values in Fig. 9a show that in dense samples ($\mu_p = 0.01$), each contact in G_{perc} transmits a higher percentage of the total percolating force when compared to less dense samples. The distribution of $\overline{\beta}$ in in Fig. 9b indicates that contacts with higher centrality are, on average, further away from sliding.

Similarly, the distribution of the mean P_{cen}, mean normalised particle size (d/d_{50}) and mean coordination number C_N of the particles in G_{perc} are presented on Fig. 10a, b and c respectively. The results show no significant differences between samples, with consistent exponential distributions of P_{cen}, i.e. few 'highly important' particles. These highly important particles are in average 10% larger than d_{50}, and have higher coordination numbers (between 6.5 and 7.0). The relation between particle importance with d/d_{50} and C_N follows a sigmoid, logistic function.

5 Micro-scale: force chains

The percolating network G_{perc} is the complete set of paths transmitting force across boundaries of the model, and thus can be decomposed into individual force chains, each of which transmits a unique value of percolating force. Each force chain is a simple path (i.e. a path without loops) of particles (and contacts between them) between the sink/source, which transmits a given force between the ribbed wall, and the opposite boundary, i.e. the force chain's percolation force. Due to the orientation of the contacts in G (and subsequently in G_{perc}), particles in each force chain have an ordered set of x coordinates (see Eq. 3). Figure 3c shows an example of five force chains extracted from G_{perc}.

Force chains are found using our implementation of the widest path problem based on Dijkstra's algorithm, which is traditionally used to find shortest paths in graphs. The widest path, also known as 'maximin' path, is defined as the path between a sink and source in the graph, which maximises the weight of the minimum-weight among the edges in such path [6]. In our context, the widest path is the force chain that transfers most percolating force between the ribbed wall and the opposite wall.

The pseudo-code of the proposed algorithm is shown in Alg. 1.

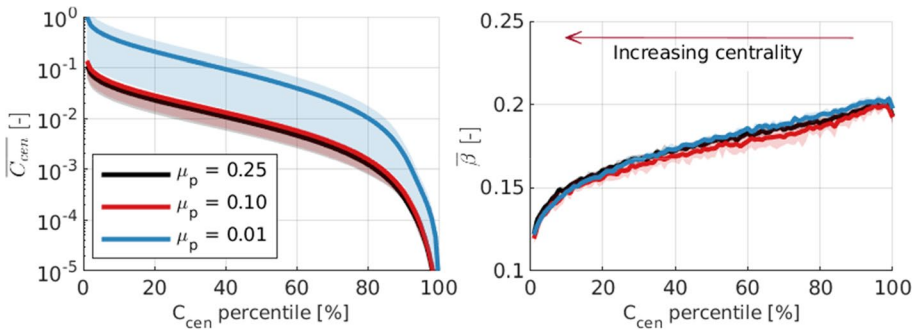

Fig. 9 **a** Mean contact centrality $\overline{C_{cen}}$, and **b** mean β, i.e. $\overline{\beta}$, of the contacts in G_{perc}, as a function of percentiles of contact centrality. Lines show the mean value across simulations and shaded regions show the inter-quartile range (IQR), namely the range between the 25th and 75th percentiles of the data from the 27 simulations

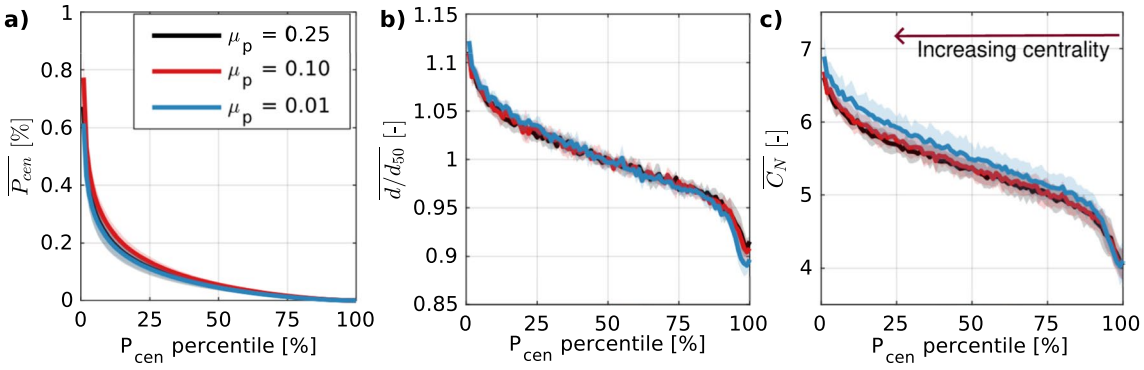

Fig. 10 **a** Mean particle centrality P_{cen}, **b** mean normalised particle size D/D_{50}, and **c** mean coordination number C_N of the particles in G_{supp}, as a function of percentiles of particle centrality. Relative particle importance calculated as percentiles of particle centrality. Lines show the mean value across simulations and shaded regions show the inter-quartile range (IQR), namely the range between the 25th and 75th percentiles of the data from the 27 simulations

Algorithm 1 Widest path, i.e. individual force chain

Data: G: Directed graph, s: source node, t: sink node
Result: cf: single force chain with: particles, contacts and percolating force
Initialization
$w \leftarrow -Inf$; # Array of width values from s to each node
$n_{par} \leftarrow []$ # array of parent nodes
$q \leftarrow$ queue of nodes to visit
while q *is not empty* **do**
  $i \leftarrow$ Retrieve element with the largest w from q
  for *each edge connected to* i **do**
    $ch \leftarrow$ child of i
    $w_c \leftarrow min(w(i), C(ch))$ # Widest path to c through this path
    if $w_c > w(ch)$ **then**
      # We have found a new widest path, update it
      $w(ch) \leftarrow w_c$
      $n_{par}(ch) \leftarrow i$
    end
  end
end
$cf \leftarrow w(t)$ # Back-track widest path from the sink node

In order to find all the force chains in the system, Alg. 1 is applied to G_{perc} sequentially. Once a force chain is found, it is recorded, and it's percolating force removed from the contacts along its path, updating the graph. Due to the significant computational cost of the algorithm, we stop the computation when only 10% of the initial percolating force remains in the percolating network. The pseudo-code of the algorithm that splits the percolating network into individual force chains is shown in Alg. 2.

Algorithm 2 Segmentation of G_{perc} into force chains

Data: G: Directed graph, s: source node, t: sink node, co Cut-off
Result: CF: array of force chains
initialization $CF \leftarrow []$ empty array of force chains
while *Percolating force* $> co$ **do**
  Find new force chain
  $i_{fc} \leftarrow WidestPath(G, s, t)$ # Find force chain
  $CF \leftarrow i_{fc}$ # Store new force chain
  $G \leftarrow$ Remove width of i_{fc} from its edges # Update graph
end

5.1 Distribution of force chains

The characterisation of the force chains in the system is done for the interval between [33, 36] mm of wall displacement (a window of 0.12 s). The interval is sampled every $1d - 4$ s, for a total of 1200 sampling points. The characteristics of the force chains were constant over time, with negligible differences between different points within the interval. The subsequent analysis on this section is based on the mean value of the quantities over the sampling interval.

The distribution of the percolating force transmitted by the force-chains is highly centralized, with the top 10% and 20% of the force chains carrying 35% and 50% of the total force percolating the sample. The overall distribution of the percolating force follows an exponential trend (see Fig. 11a), similar to the distributions of particle importance (in Fig. 10a) and contact importance (in Fig. 9a).

The overall system centrality (also called the concentration or inequality) is measured using the unitary Gini coefficient g_c. A g_c value of zero corresponds to a system where all

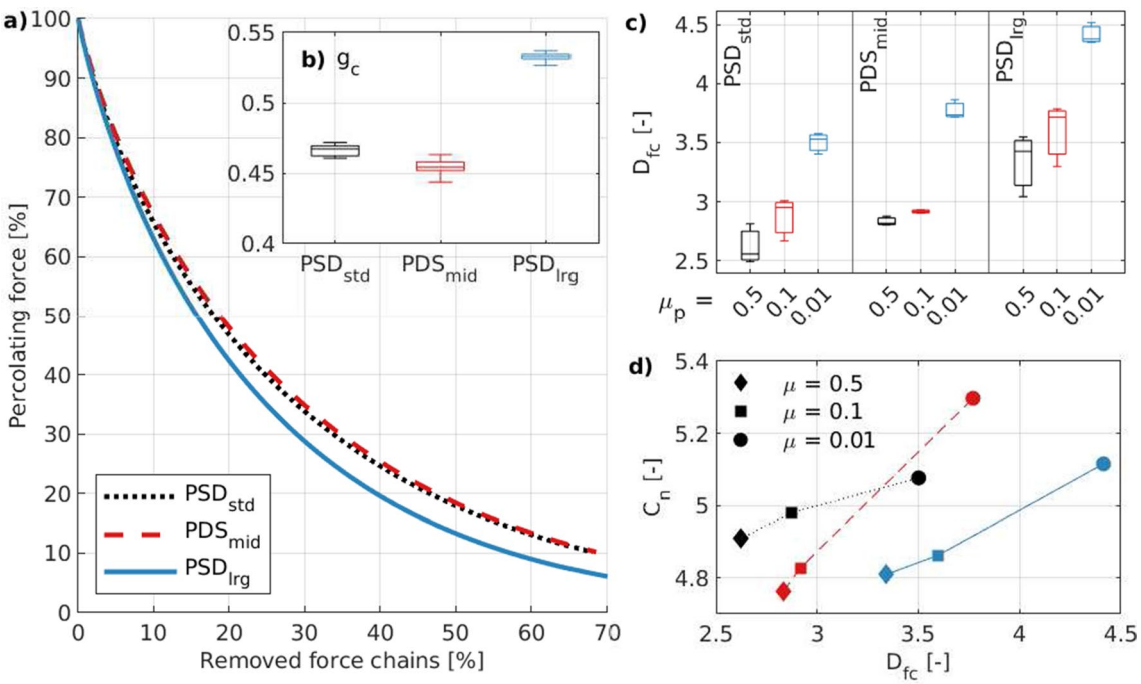

Fig. 11 **a** Distribution of percolating force in force chains, plotted as a survival plot. **b** Gini's inequality coefficient (gc) of the percolating force distributions as a function of PSD; 9 values per boxplot. **c** Density of force chains D_{fc} as a function of GDS and μ_p; 3 values per boxplot. **d** Comparison between D_{fc} and average coordination number C_N in the network

the force chains carry the same force (i.e. homogeneous system), and the value grows as the difference between forces increase (i.e. increased system centrality). Figure 11b summarizes the distribution of g_c as a function of *PSD*, variable that showed the largest statistical influence. Results indicate that samples with larger particles 'depend' more heavily on a relatively few number of strong force chains, whereas similar samples with smaller particles distribute the load among force chains more evenly.

The 'density' of force chains D_{fc} in the system is calculated as:

$$N_{pw} = \frac{H_m \cdot D_m}{d_{50}^2}$$
$$D_{fc} = \frac{N_{fc}}{N_{pw}} \quad (4)$$

where N_{pw} is the average number of particles in contact with the ribbed wall, and N_{fc} is the number of force chains that account for 90% of the total percolating force in the system (i.e., the maximum flow value transmitted by G_{perc}).

Figure 11c shows the distribution of D_{fc} for the 27 simulations as a function of *PSD* and μ_p. Figure 11d shows a direct relationship between the density of force chains per unit area D_{fc} and the average coordination number C_N. This relationship is expected, as denser arrays have more contacts between particles, facilitating the creation of more pathways for force transmission. However, the range of C_N does not vary with particle size, indicating that the increase in D_{fc} with increasing PSD is not due to higher coordination numbers in the system, but instead, due a higher fraction of particles/contacts in G_{perc}, in agreement with Fig. 4.

These results indicate that sample density, and K_o increase the density of force chains in the system, while making it more centralised (in terms of g_c). These findings agree with the trends observed in Fig. 2, linking the increase in the mobilised stress in the material with an increased force chain density and system centrality.

5.2 Life-span of force chains

The longevity or duration of force chains during the induced shear deformation, a matter also addressed by [28], is considered next. We measure the duration of each force chain in the system within the same interval: [33, 36] mm of wall displacement (0.12 s), sampled every $1d - 4$ s, for a total of 1200 points.

The duration of a force chain in the contact network is equal to the sample interval ($1d - 4$ s) times the number of consecutive intervals where the same force chain can be found. Each force chain fc_m is identified by as the set of contacts that form it, namely $fc_m : \{c_{i,j}, c_{j,k}, ...\}$, where $c_{i,j}$ is the contact between particles i and j. The similarity index, a modified version of the overlap coefficient [60], is used as the criteria to compare force chains at different times:

$$Sim_{(m,n)} = \frac{2(|\, fc_m \cap fc_n \,|)}{|\, fc_m \,| + |\, fc_n \,|} \quad (5)$$

The similarity index of force chains fc_m and fc_n, namely $Sim_{(m,n)}$, is calculated as the number of contacts common to both chains, divided by the average number of contacts in fc_m and fc_n, as shown in Eq. 5. If two force chains in consecutive time steps (say fc_m and fc_n) have $Sim_{(m,n)} \leq 75\%$, we consider them to be the same force chain, and increase its

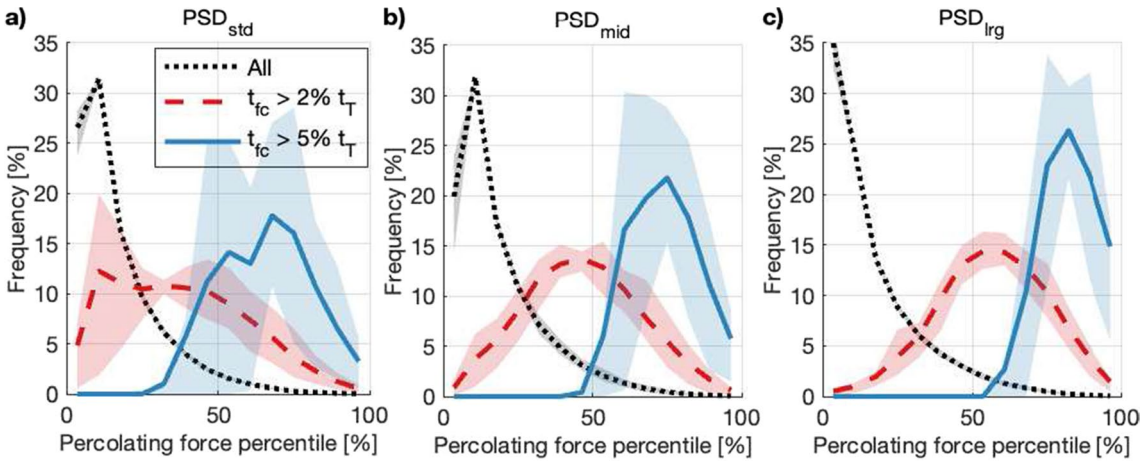

Fig. 12 Distribution of percolating force in force chains by duration. Groups show the distribution among the entire set of force chains ('All'), and among those with a duration above 2% and 5% of the time interval analysed $T_t = 0.12$ s. Lines and shaded regions show the mean value and inter-quartile range (IQR) of the data in each group

duration. In the vicinity of the start/end of the time window studied the algorithm may underestimate the duration of the force chains.

Once the duration of the force chains in the system was calculated, we studied the distribution of the force-chains' percolating force for three groups of different duration: the baseline group contains all the force chains in the system regardless of their duration, namely 'All'; the second group includes only the force-chains with a duration above 2% of the analysed time interval, namely $t_{fc} > 2\%t_T$; similarly, the third group includes the force chains with a duration above 5% of the analysed time window, namely $t_{fc} > 5\%t_T$.

The results in Fig. 12 show that force chains with longer life-spans, i.e. long-lived force chains, are (in average) stronger than short-lived chains. These results are in agreement with Fig. 9, as strong, 'important' contacts in the long-lived force chains have lower values of $\overline{\beta}$ (less prone to sliding), explaining their increased duration.

Moreover, the comparison between different PSDs in Fig. 12 shows that in samples with PSD_{lrg}, long-lived chains are comparatively stronger that force chains of the same duration with smaller PSD. This observation is supported by the increased centrality of systems with larger particles shown in Fig. 11b.

6 Conclusions

This contribution has proposed new algorithms to: (1) extract the fully-connected set of percolating contacts (G_{perc}) that controls the stress/deformation response of granular systems, and to (2) decompose G_{perc} into the underlying set of force chains that form it. These algorithms were then applied to a particular scenario, the response of granular materials to shear deformation induced by a ribbed interface moving at a constant speed and the steady-state response of the material was considered here. The data show that granular materials behave as highly centralised systems, where the mechanical response to shear deformation is ultimately controlled by a small set of strong and long-lived force chains.

In Sect. 4, we proposed a partitioning method that splits the contact network into a stress-carrying percolating network G_{perc} and a supporting sub-network G_{supp}. This approach is not the first to use the maximum flow algorithm, but (to the best of our knowledge) is the first to use directed edges with a physically based capacity (transmitted force). By doing so, G_{perc} captures the force percolating between boundaries, and all the paths that transmit it. Thus, this partitioning method has a stronger fundamental basis than the commonly used approach that splits the force network by considering the mean force.

Results show that G_{perc} contains 35–65% of the contacts (see Fig. 4), but carries most of the stress in the sample ($> 80\%$, see Fig. 6). Interestingly, it was found that G_{perc} has a larger proportion of large particles, but both sub-networks include particles across the entire PSD. Similarly, the contact-force distribution shows that G_{perc} has stronger contact-forces in average, but both sub-networks contain weak to strong contacts. The major principal stress orientation shows that G_{perc} re-orientates at an angle between 35° - 55° as a response to the ribbed wall movement, while G_{supp} carries little stress and remains oriented along the vertical direction.

In Sect. 5, we proposed a method to split G_{perc} into individual force chains based on a new implementation of the widest path problem. With this method, each resulting force chain is an aligned set of particles/contacts in G_{perc} that transmits a specific value of percolating force.

The force chains in the system form a highly centralised system that follows an exponential distribution, with a small number of strong and long-lived force chains, and a large number of weaker, ephemeral chains. These observations have been related to the stress-deformation response of the system, showing that systems with a more centralised distribution of contacts and higher density of force chains are able to mobilise higher mobilised stress ratios during shear deformation, providing micro-mechanical insight to previous laboratory and in-situ testing observations.

The methods discussed here may be applicable to a wide range of applications in geomechanics, including boundary problems, monotonic/cyclic loading and even pore network modeling. Future studies may also focus on the role of polydispersity and particle shape in the centrality and density of the force chains in the material. Understanding the role of the particle-scale properties in the behavior of force chains may allow to design granular materials that maximise the performance or resiliency of the system, i.e. the capacity to accommodate changes in loading into the existent network of force chains, under specific loading cases.

Funding This material is based upon work supported by the National Science Foundation under Grant No. 1935548. Any opinions, findings, and conclusions or recommendations expressed in this material are those of the author(s) and do not necessarily reflect the views of the National Science Foundation. Funding was provided by a project entitled 'SitS NSF UKRI: Rapid deployment of multi-functional modular sensing systems in the soil' by the United Kingdom Research and Innovation (UKRI) agency, under NERC Grant NE/T010983/1. The financial support is gratefully acknowledged. For the purpose of open access, the author has applied a Creative Commons Attribution (CC BY) license to any Author Accepted Manuscript version arising.

Data availability The datasets generated during and/or analysed during the current study are available from the corresponding author on reasonable request.

Declarations

Conflict of interest The authors declare that they have no known competing financial interests or personal relationships that could have appeared to influence the work reported in this paper.

References

1. Radjai, F., Jean, M., Moreau, J.-J., Roux, S.: Force distributions in dense two-dimensional granular systems. Phys. Rev. Lett. **77**(2), 274 (1996). https://doi.org/10.1103/PhysRevLett.77.274
2. Thornton, C., Antony, S.J.: Quasistatic deformation of particulate media. Philos. Trans. R. Soc. Lond. Ser. A: Math. Phys. Eng. Sci. **356**(1747), 2763–2782 (1998). https://doi.org/10.1098/RSTA.1998.0296
3. Antony, S.J.: Link between single-particle properties and macroscopic properties in particulate assemblies: role of structures within structures. Philos. Trans. R. Soc. Lond. Ser. A: Math. Phys. Eng. Sci. **365**(1861), 2879–2891 (2007). https://doi.org/10.1098/RSTA.2007.0004
4. Barreto, D., O'Sullivan, C.: The influence of inter-particle friction and the intermediate stress ratio on soil response under generalised stress conditions. Granul. Matter **14**(4), 505–521 (2012). https://doi.org/10.1007/s10035-012-0354-z
5. Tordesillas, A.: Force chain buckling, unjamming transitions and shear banding in dense granular assemblies. Phil. Mag. **87**(32), 4987–5016 (2007). https://doi.org/10.1080/14786430701594848
6. Walker, D.M., Tordesillas, A., Thornton, C., Behringer, R.P., Zhang, J., Peters, J.F.: Percolating contact subnetworks on the edge of isostaticity. Granul. Matter **13**(3), 233–240 (2011). https://doi.org/10.1007/S10035-011-0250-Y
7. O'Sullivan, C., Wadee, M.A., Hanley, K.J., Barreto, D.: Use of DEM and elastic stability analysis to explain the influence of the intermediate principal stress on shear strength. Geotechnique **63**(15), 1298–1309 (2013). https://doi.org/10.1680/geot.12.P.153
8. Radjaï, F.: Features of force transmission in granular media. Powders Grains **2001**, 157–160 (2020). https://doi.org/10.1201/9781003077497-40
9. Radjai, F., Wolf, D.E., Jean, M., Moreau, J.J.: Bimodal character of stress transmission in granular packings. Phys. Rev. Lett. **80**(1), 61 (1998). https://doi.org/10.1103/PhysRevLett.80.61
10. Tordesillas, A., Muthuswamy, M.: On the modeling of confined buckling of force chains. J. Mech. Phys. Solids **57**(4), 706–727 (2009). https://doi.org/10.1016/J.JMPS.2009.01.005
11. Seguin, A.: Experimental study of some properties of the strong and weak force networks in a jammed granular medium. Granul. Matter **22**(2), 1–8 (2020). https://doi.org/10.1007/S10035-020-01015-Z
12. Ostojic, S., Somfai, E., Nienhuis, B.: Scale invariance and universality of force networks in static granular matter. Nature **439**(7078), 828–830 (2006). https://doi.org/10.1038/nature04549
13. Huang, X., Hanley, K.J., O'Sullivan, C., Kwok, C.Y.: Implementation of rotational resistance models: a critical appraisal. Particuology **34**, 14–23 (2017). https://doi.org/10.1016/J.PARTIC.2016.08.007
14. Papadopoulos, L., Porter, M.A., Daniels, K.E., Bassett, D.S.: Network analysis of particles and grains. J. Complex Netw. **6**(4), 485–565 (2018). https://doi.org/10.1093/COMNET/CNY005
15. Ardanza-Trevijano, S., Zuriguel, I., Arévalo, R., Maza, D.: Topological analysis of tapped granular media using persistent homology. Phys. Rev. E Stat. Nonlinear Soft Matter Phys. (2014). https://doi.org/10.1103/PHYSREVE.89.052212
16. Luding, S., Taghizadeh, K., Cheng, C., Kondic, L.: Understanding slow compression and decompression of frictionless soft granular matter by network analysis. Soft Matter **18**(9), 1868–1884 (2022). https://doi.org/10.1039/D1SM01689J
17. Kramar, M., Cheng, C., Basak, R., Kondic, L.: On intermittency in sheared granular systems (2021) arXiv:2112.11344
18. Bassett, D.S., Owens, E.T., Daniels, K.E., Porter, M.A.: Influence of network topology on sound propagation in granular materials. Phys. Rev. E **86**(4), 041306 (2012)
19. Walker, D.M., Tordesillas, A.: Taxonomy of granular rheology from grain property networks. Phys. Rev. E **85**(1), 011304 (2012)
20. Tordesillas, A., Walker, D.M., Andò, E., Viggiani, G.: Revisiting localized deformation in sand with complex systems. Proc. R. Soc. A: Math. Phys. Eng. Sci. **469**(2152), 20120606 (2013)
21. Walker, D.M., Tordesillas, A., Pucilowski, S., Lin, Q., Rechenmacher, A.L., Abedi, S.: Analysis of grain-scale measurements of sand using kinematical complex networks. Int. J. Bifurc. Chaos **22**(12), 1230042 (2012)
22. Tordesillas, A., Cramer, A., Walker, D.M.: Minimum cut and shear bands. In: AIP Conference Proceedings, vol. 1542, pp. 507–510. American Institute of PhysicsAIP (2013). https://doi.org/10.1063/1.4811979
23. Tordesillas, A., Tobin, S.T., Cil, M., Alshibli, K., Behringer, R.P.: Network flow model of force transmission in unbonded and bonded granular media. Phys. Rev. E Stat. Nonlinear Soft Matter Phys. **91**(6), 062204 (2015). https://doi.org/10.1103/PhysRevE.91.062204
24. Tordesillas, A., Pucilowski, S., Tobin, S., Kuhn, M.R., Andò, E., Viggiani, G., Druckrey, A., Alshibli, K.: Shear bands as bottlenecks in force transmission. EPL (Europhys. Lett.) **110**(5), 58005 (2015). https://doi.org/10.1209/0295-5075/110/58005
25. Peters, J.F., Muthuswamy, M., Wibowo, J., Tordesillas, A.: Characterization of force chains in granular material. Phys. Rev. E **72**(4), 041307 (2005). https://doi.org/10.1103/PhysRevE.72.041307
26. Tian, J., Liu, E.: Influences of particle shape on evolutions of force-chain and micro-macro parameters at critical state for granular materials. Powder Technol. **354**, 906–921 (2019). https://doi.org/10.1016/j.powtec.2019.07.018
27. Bassett, D.S., Owens, E.T., Porter, M.A., Manning, M.L., Daniels, K.E.: Extraction of force-chain network architecture in granular materials using community detection. Soft Matter **11**(14), 2731–2744 (2015). https://doi.org/10.1039/C4SM01821D
28. Kuhn, M.R., Asce, M.: Contact transience during slow loading of dense granular materials. J. Eng. Mech. **143**(1), 4015003 (2015). https://doi.org/10.1061/(ASCE)EM.1943-7889.0000992
29. Tordesillas, A., Shi, J., Tshaikiwsky, T.: Stress-dilatancy and force chain evolution. Int. J. Numer. Anal. Methods Geomech. **35**(2), 264–292 (2011). https://doi.org/10.1002/NAG.910
30. Tordesillas, A., Steer, C.A.H., Walker, D.M.: Force chain and contact cycle evolution in a dense granular material under shallow

penetration. Nonlinear Process. Geophys. **21**(2), 505–519 (2014). https://doi.org/10.5194/NPG-21-505-2014
31. Wang, W., Gu, W., Liu, K.: Force chain evolution and force characteristics of shearing granular media in Taylor–Couette geometry by DEM. Tribol. Trans. **58**(2), 197–206 (2015). https://doi.org/10.1080/10402004.2014.943829
32. Papadopoulos, L., Puckett, J.G., Daniels, K.E., Bassett, D.S.: Evolution of network architecture in a granular material under compression. Phys. Rev. E **94**(3), 032908 (2016). https://doi.org/10.1103/PhysRevE.94.032908
33. DeJong, J.T., Westgate, Z.J.: Role of initial state, material properties, and confinement condition on local and global soil-structure interface behavior. J. Geotech. Geoenviron. Eng. **135**(11), 1646–1660 (2009). https://doi.org/10.1061/(ASCE)1090-0241(2009)135:11(1646)
34. DeJong, J.T., Frost, J.D., Cargill, P.E.: Effect of surface texturing on CPT friction sleeve measurements. J. Geotech. Geoenviron. Eng. **127**(2), 158–168 (2001). https://doi.org/10.1061/(ASCE)1090-0241(2001)127:2(158)
35. Ferdowsi, B., Griffa, M., Guyer, R.A., Johnson, P.A., Marone, C., Carmeliet, J.: Microslips as precursors of large slip events in the stick-slip dynamics of sheared granular layers: a discrete element model analysis. Geophys. Res. Lett. **40**(16), 4194–4198 (2013). https://doi.org/10.1002/grl.50813
36. Rouet-Leduc, B., Hulbert, C., Lubbers, N., Barros, K., Humphreys, C.J., Johnson, P.A.: Machine learning predicts laboratory earthquakes. Geophys. Res. Lett. **44**(18), 9276–9282 (2017). https://doi.org/10.1002/2017GL074677
37. Martinez, A., Frost, J.D.: The influence of surface roughness form on the strength of sand-structure interfaces. Géotech. Lett. **7**(1), 104–111 (2017). https://doi.org/10.1680/jgele.16.00169
38. Martinez, A., Frost, J.D.: Particle-scale effects on global axial and torsional interface shear behavior. Int. J. Numer. Anal. Methods Geomech. **41**(3), 400–421 (2017). https://doi.org/10.1002/nag.2564
39. Su, J.: Advancing multi-scale modeling of penetrometer insertion in granular materials. Ph.D. Thesis, Georgia Institute of Technology (2019)
40. Hebeler, G.L., Martinez, A., Frost, J.D.: Interface response-based soil classification framework. Can. Geotech. J. **55**(12), 1795–1811 (2018). https://doi.org/10.1139/cgj-2017-0498
41. Plimpton, S.: Fast parallel algorithms for short-range molecular dynamics. J. Comput. Phys. **117**(1), 1–19 (1995). https://doi.org/10.1006/jcph.1995.1039
42. Group, I.C.: PFC3D: Particle Flow Code in Three Dimensions User's Guide, 4th edition. Itasca Consulting Group, Minneapolis (2008)
43. Potyondy, D.O., Cundall, P.A.: A bonded-particle model for rock. Int. J. Rock Mech. Min. Sci. **41**(8), 1329–1364 (2004). https://doi.org/10.1016/J.IJRMMS.2004.09.011
44. O'Sullivan, C.: Advancing geomechanics using DEM. In: Proceedings of the TC105 ISSMGE international symposium on geomechanics from micro to macro. Taylor & Francis Group, Cambridge (2014)
45. Yang, J., Sze, H.Y.: Cyclic behaviour and resistance of saturated sand under non-symmetrical loading conditions. Géotechnique **61**(1), 59–73 (2011). https://doi.org/10.1680/geot.9.P.019
46. Hryciw, R.D., Irsyam, M.: Behavior of sand particles rigid ribbed inclusions during shear. Soils Found. **33**(3), 1–13 (1993). https://doi.org/10.3208/sandf1972.33.3_1
47. da Cruz, F., Emam, S., Prochnow, M., Roux, J.-N., Chevoir, F.: Rheophysics of dense granular materials: discrete simulation of plane shear flows. Phys. Rev. E **72**, 021309 (2005). https://doi.org/10.1103/PhysRevE.72.021309
48. Lu, Q., Randolph, M.F., Hu, Y., Bugarski, I.C.: A numerical study of cone penetration in clay. Geotechnique **54**(4), 257–267 (2004). https://doi.org/10.1680/GEOT.2004.54.4.257/ASSET/IMAGES/SMALL/GEOT54-257-F19.GIF
49. Janda, A., Ooi, J.Y.: DEM modeling of cone penetration and unconfined compression in cohesive solids. Powder Technol. **293**, 60–68 (2016). https://doi.org/10.1016/J.POWTEC.2015.05.034
50. Hebeler, G.L., Martinez, A., Frost, J.D.: Shear zone evolution of granular soils in contact with conventional and textured CPT friction sleeves. KSCE J. Civ. Eng. **20**(4), 1267–1282 (2016). https://doi.org/10.1007/s12205-015-0767-6
51. Luding, S., Lätzel, M., Volk, W., Diebels, S., Herrmann, H.J.: From discrete element simulations to a continuum model. Comput. Methods Appl. Mech. Eng. **191**(1–2), 21–28 (2001). https://doi.org/10.1016/S0045-7825(01)00242-0
52. Yu, H.S., Mitchell, J.K., Member, H.: Analysis of cone resistance: review of methods. J. Geotech. Geoenviron. Eng. **124**(2), 140–149 (1998). https://doi.org/10.1061/(ASCE)1090-0241(1998)124:2(140)
53. Salgado, B.R., Member, A., Boulanger, R.W., Mitchell, J.K., Member, H.: Lateral stress effects on CPT liquefaction resistance correlations. J. Geotech. Geoenviron. Eng. **123**(8), 726–735 (1997). https://doi.org/10.1061/(ASCE)1090-0241(1997)123:8(726)
54. Salgado, R., Mitchell, J., Jamiolkowski, M.: Cavity expansion and penetration resistance in sand. J. Geotech. Geoenviron. Eng. **123**(4), 344–354 (1997)
55. Moss, R.E., Seed, R.B., Olsen, R.S.: Normalizing the CPT for Overburden Stress. J. Geotech. Geoenviron. Eng. **132**(3), 378–387 (2006). https://doi.org/10.1061/(ASCE)1090-0241(2006)132:3(378)
56. Butlanska, J., Arroyo, M., Gens, A.: 3D dem simulations of CPT in sand. In: Geotechnical and Geophysical Site Characterization: Proceedings of the 4th International Conference on Site Characterization ISC-4, vol. 1, pp. 817–824 (2013). Taylor & Francis Books Ltd
57. West, D.B., et al.: Introduction to Graph Theory, vol. 2. Prentice Hall, Upper Saddle River (2001)
58. MATLAB: 9.7.0.1190202 (R2019b). The MathWorks Inc., Natick (2018)
59. Imole, O.I., Wojtkowski, M., Magnanimo, V., Luding, S.: Micro-macro correlations and anisotropy in granular assemblies under uniaxial loading and unloading. Phys. Rev. E **89**(4), 042210 (2014). https://doi.org/10.1103/PhysRevE.89.042210
60. Wang, X., De Baets, B., Kerre, E.: A comparative study of similarity measures. Fuzzy Sets Syst. **73**(2), 259–268 (1995)